Editors' Suggestion

Time-gated optical spectroscopy of field-effect-stimulated recombination via interfacial point defects in fully processed silicon carbide power MOSFETs

Maximilian W. Feil,[1,2,*] Magdalena Weger,[3] Hans Reisinger,[2] Thomas Aichinger,[4] André Kabakow,[2] Dominic Waldhör,[1] Andreas C. Jakowetz,[2] Sven Prigann,[2] Gregor Pobegen,[3] Wolfgang Gustin,[2] Michael Waltl,[5] Michel Bockstedte,[6] and Tibor Grasser[1]

[1] *Institute for Microelectronics, TU Wien, Gußhausstraße 27–29/E360, 1040 Vienna, Austria*

[2] *Infineon Technologies AG, Am Campeon 1–15, 85579 Neubiberg, Germany*

[3] *KAI GmbH, Europastraße 8, 9524 Villach, Austria*

[4] *Infineon Technologies Austria AG, Siemensstraße 2, 9500 Villach, Austria*

[5] *Christian Doppler Laboratory for Single-Defect Spectroscopy at the Institute for Microelectronics, TU Wien, Gußhausstraße 27–29/E360, 1040 Vienna, Austria*

[6] *Johannes Kepler University Linz, Altenberger Straße 69, 4040 Linz, Austria*

(Received 11 April 2024; accepted 1 July 2024; published 30 August 2024)

Fully processed SiC power MOSFETs emit light during switching of the gate terminal, while the drain and source terminals are both grounded. The emitted photons are caused by defect-assisted recombination of electrons and holes at the 4*H*-SiC/SiO_2 interface, and can be detected through the SiC substrate. Here we present time-gated spectroscopic characterization of these interfacial point defects. Unlike in previous studies, the devices were opened in such a way that the drain contact remained electrically active. A separate examination of the photons emitted at the rising and falling transitions of the gate-source voltage enabled the extraction of two different spectral components. One of these components consists of a single transition with phonon replicas of a local vibrational mode with an astonishingly high energy of 220 meV—well above the highest phonon modes in 4*H*-SiC and SiO_2 of 120 and 137 meV, respectively. On the basis of a quantum mechanical model, we successfully fitted its emission spectrum and assigned it to donor-acceptor-pair recombination involving a carbon-cluster-like defect. Other transitions were assigned to $EH_{6/7}$-assisted, EK_2-D, and nitrogen-aluminum donor-acceptor-pair recombination. Because of the relevance of these defects in the operation of SiC MOSFETs, these insights will contribute to improved reliability and performance of these devices.

DOI: 10.1103/PhysRevApplied.22.024075

I. INTRODUCTION

Wide-band-gap semiconductors, such as silicon carbide (SiC), gallium nitride (GaN), and diamond have rapidly moved into the focus of both academic research and industrial development over the past few years [1–3]. They are becoming increasingly important and are revolutionizing power electronics by enabling reliable power conversion with higher energy efficiency at reduced weight and size compared with conventional silicon (Si)-based technologies [4–6]. In particular 4*H*-SiC has proven to be the premier wide-band-gap solution at high power and voltages beyond 600 V, which is required by many renewable-energy applications and emission-free vehicles [7,8].

However, 4*H*-SiC MOSFETs exhibit a roughly-100-times-higher defect density at the interface between 4*H*-SiC and its native oxide SiO_2 compared with the well-studied Si/SiO_2 interface [9]. Because of the presence of carbon and the use of nitrogen-based annealing techniques [10,11], a variety of new defects can occur in comparison with Si-based devices [12–14]. These defects can act as traps for charge carriers from both the valence band and the conduction band of SiC. This trapping and detrapping is highly dynamic, with time constants down to nanoseconds [15–17]. The time constants are determined by electric field–dependent activation energies for charge capture and emission, as given by the nonradiative multiphonon (NMP) theory [18–20]. These fast trapping processes do not lead to long-term drifts of the threshold voltage V_{th}, but lead to a hysteresis in all device characteristics, such as the transfer or the capacitance-voltage (*C-V*) characteristics [21]. Besides this, defect-assisted recombination and subsequently enhanced defect reactions were recently held responsible for a degradation mechanism referred to as "gate switching instability" [22–24]. Identifying defects that are involved in the hysteresis and recombination processes at the

*Contact author: maximilian.feil@infineon.com

4*H*-SiC/SiO_2 interface is therefore elementary for improving the reliability and performance of these devices. For this purpose, a variety of different techniques to characterize and investigate these defects in SiC devices have been developed, ranging from purely electrical techniques (measure-stress-measure, capacitance-voltage, deep-level transient spectroscopy, and charge pumping) to optical techniques (photoluminescence and single-photon spectroscopy) and magnetic resonance techniques—detected either electrically or optically [25,26].

Besides these techniques, Stahlbush *et al.* [27,28] and Macfarlane and Stahlbush [29] observed that 4*H*-SiC MOSFETs emit light during switching of the gate terminal, while the drain and source terminals were both kept grounded. Hereby, the field effect stimulated radiative recombination of electrons and holes via defects at the SiC/SiO_2 interface. We recently confirmed the relation between this light emission and the defects of interest in device operation by correlating the transient V_{th} shift with the light emission [30,31]. This was investigated further by Weger *et al.* [32,33], who demonstrated a correlation between the recombination current of a charge-pumping experiment and the intensity of a part of the emission spectrum. However, a clear identification of the defects involved was not possible.

Here we contribute to the identification by setting up an experiment that allows time-gated spectral detection of the emitted photons during gate switching of a fully processed 4*H*-SiC power MOSFET (see Fig. 1). The time gating allowed us to distinguish between the recombination events occurring at the rising and falling transitions of the gate-source voltage V_{GS}. Depending on whether the rising transition or the falling transition is being considered, the underlying mechanisms differ considerably, which makes their separation important. At the interface, the distinction between the two transitions arises from the reverse chronological sequence of electron (inversion) and hole (accumulation) presence. This led to the extraction of two major spectral components. One of them consists of a transition with a zero-phonon line (ZPL) of 2.53 eV and phonon replicas with a spacing of 220 meV. On the basis of a simple model of a one-dimensional harmonic approximation of the Born-Oppenheimer potentials involved, inhomogeneous broadening, and transition rates determined by Fermi's golden rule [see Fig. 2(a)], we identified this component as donor-acceptor-pair (DAP) recombination involving a carbon-cluster-like defect. This defect is responsible for the observed phonon replicas that stem from a high-energy local vibrational mode (LVM), the energy of which is considerably greater than the energies of the highest phonon modes in 4*H*-SiC and SiO_2 of 120 and 137 meV, respectively. This makes the LVM a unique signature of this defect. Besides that, we could further assign an emission peak at 1.55 eV to the $EH_{6/7}$ defect and the other component at the rising transition to other DAP recombination paths, including EK_2-D and nitrogen-aluminum DAP recombination. This other component occurring at the rising transition could be stimulated by forward biasing the body diode.

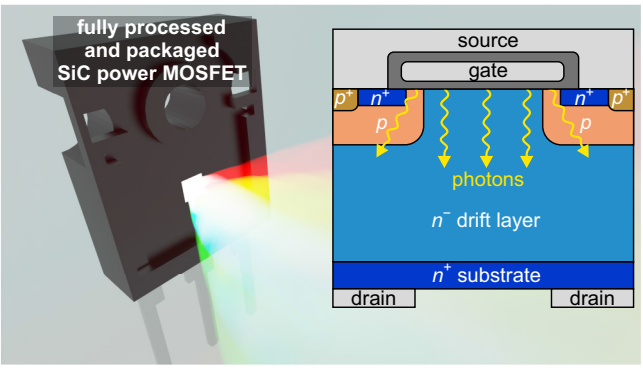

FIG. 1. Light emission from a SiC power MOSFET switched between inversion and accumulation. The light is created via defect-assisted recombination of electrons and holes at the SiC/SiO_2 interface. Fully processed and packaged SiC power MOSFETs can be opened and prepared for optical inspection, which includes a partial removal of the drain metallization.

First, we describe the experimental method used in Sec. II, followed by a comparison of the emission spectra occurring at the rising and falling transitions, including their relation to the emission spectrum of the forward-biased body diode in Sec. III. We investigate the dependence of the emission spectrum on the bias levels in Sec. IV and on the frequency and duty cycle in Sec. V. We show the dependence on the transition times of V_{GS} in Sec. VI, followed by the temporal evolution of the emission spectrum over the entire V_{GS} period in Sec. VII. Finally, in Sec. VIII we discuss the experimental results in the context of recent experimental and theoretical studies from the literature.

II. METHODS

We used commercially available, fully processed, *n*-channel 4*H*-SiC power MOSFETs with a planar double-diffused MOS design and in a transistor-outline package. In these devices, the 4*H*-SiC/SiO_2 interface is located at the (0001) face of the 4*H*-SiC crystal. The three pins of the transistor-outline package are used to contact the gate, drain, and source terminals. The drain terminal is located at the back side of the chip. We opened the devices from the back for direct optical detection through the SiC substrate and epitaxial layer to enable the photons created at the 4*H*-SiC/SiO_2 interface to leave the device without being disturbed [34]. We removed the copper lead frame using a wet chemical process with nitric acid and etched away the solder on the chip using aqua regia. Finally, we polished

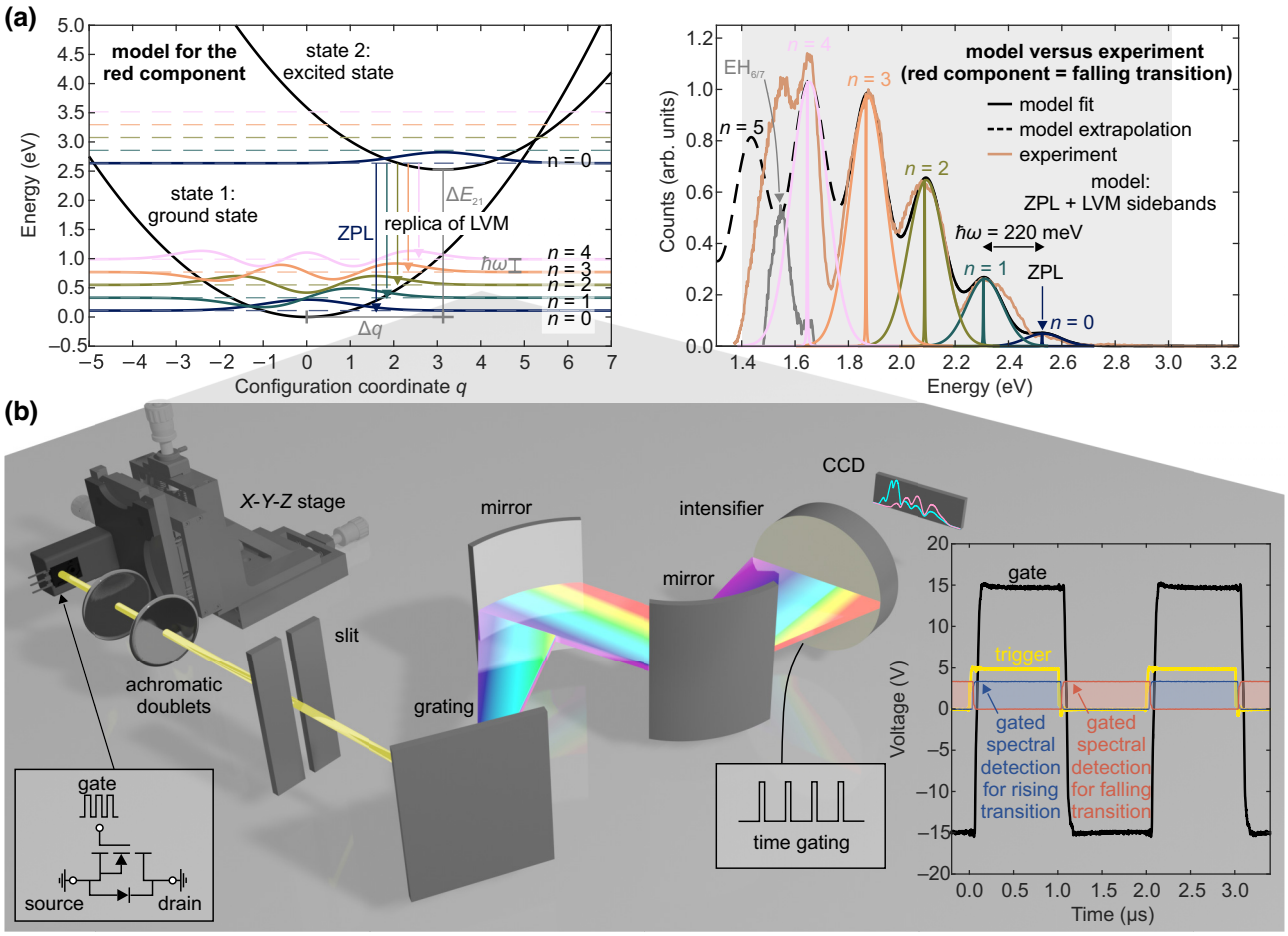

FIG. 2. Experimental setup and comparison between model and experiment of the emission spectrum of the falling transition (red component). (a) The model for the red component consists of a harmonic approximation of the Born-Oppenheimer potentials of two electronic states, between which radiative transitions can emanate from the vibrational ground state of state 2 to the lowest five vibrational states of state 1. This includes the ZPL and four LVM sidebands. The parameters of the potentials can be obtained by fitting the model to an emission spectrum. The right plot shows a comparison between the theoretical emission spectrum from the model in the left plot (obtained by fitting) and the experimentally observed emission spectrum at the falling V_{GS} transition (red component). The gray background indicates the trusted energy region, where the detected spectrum is fully calibrated with respect to intensity and wavelength (see Appendix A). (b) Experimental setup for time-gated optical spectroscopy. The inset at the bottom right exemplarily shows the timing of a typical measurement that distinguishes between light emission from the falling transition and light emission from the rising transition—the corresponding spectra are presented in Fig. 3.

off the back-side metallization with diamond paste. Unlike in previous studies, this preparation was performed such that some of the drain metallization remained functional to provide electrical control over the potential of the highly doped *n*-type region at the drain contact.

The MOSFET was subsequently mounted on a 3D-printed holder, which was in turn mounted on an *X*-*Y*-*Z* translation stage with differential adjusters [see Fig. 2(b)]. The package was fixed with a screw and its pins were connected via short cables to a custom ultrafast bias temperature instability setup [15,35]. All the experiments were conducted at room temperature. For the experiments presented in Sec. VI, where we separately varied the rise time and the fall time of the V_{GS} waveform, we used an Agilent 4156C precision semiconductor parameter analyzer with a 41501B pulse generator and expander unit.

The emitted light was coupled via two achromatic doublet lenses (diameter 2.54 cm, focal lengths 30 and 100 mm) into the slit of a Teledyne Princeton Instruments IsoPlane 160 imaging spectrograph (Schmidt-Czerny-Turner design) with a grating of 150 mm^{-1} and a 500-nm blaze wavelength combined with silver-coated mirrors [see Fig. 2(b)]. The doublet lenses featured an antireflection coating for wavelengths ranging from 400 to 1100 nm. For time gating the spectral detection, we used a Teledyne Princeton Instruments PI-MAX4 (PM4-256f-HR-FG-18-P43) intensified-charge-coupled-device (ICCD) camera that was attached to the spectrograph.

The benefit of using an ICCD camera is its intensifier that can be time-gated in such a way that the CCD is exposed to the light only within the gate time window (t_{gate}) (minimum 3 ns). The time window starts after a defined gate delay time ($t_{gate,del}$) (minimum 25 ns) following the transition of a trigger pulse. Fifty nanoseconds after the trigger signal, the ultrafast bias temperature instability setup switches the gate either from low level (V_L) to high level (V_H) or the other way around [see the inset in Fig. 2(b)].

This setup allowed time-gated spectral detection in the range from 400 to 900 nm with a single exposure of the CCD. In all experiments, the amplification of the intensifier was set to unity. We performed both wavelength and intensity calibration, which is described in detail in Appendix A. Finally, all recorded spectra were transformed from wavelength into energy space by means of a Jacobian transformation [36].

III. RISING VERSUS FALLING TRANSITION

The light emission occurs at the transitions of V_{GS} [30,31]. Time gating the spectral detection with an ICCD camera provides a time resolution that allows the detection of the light emission from the rising transition or the falling V_{GS} transition only.

To separate the emission spectra of the rising and falling transitions, we used continuous gate switching at 500 kHz between $V_L = -15$ V and $V_H = 15$ V with 50% duty cycle and a rise time (t_{rise}) and a fall time (t_{fall}) of 50 ns. We chose $t_{gate,del} = 25$ ns and $t_{gate} = 1\,\mu$s to fully capture the light emission of the respective V_{GS} transition, while rejecting the light emission of the other V_{GS} transition. In a separate experiment, we investigated the light emission that occurs when a forward bias is applied to the body diode. As the underlying recombination events occur dominantly in the bulk of the 4*H*-SiC crystal, we can use the resulting spectrum to compare the dominant recombination paths in the bulk with the events found closer to the 4*H*-SiC/SiO_2 interface that are triggered by switching of the gate terminal. We measured the spectra from the body diode with a forward bias corresponding to a constant current of 40 mA.

The spectra obtained on switching the gate terminal are shown in Fig. 3. First, it is notable that the spectrum at the rising transition covers a broader range of energy up to about 3 eV, whereas the spectrum at the falling transition disappears for energies above 2.65 eV. We found good agreement between the two emission spectra for energies in the range from 1.6 to 2.0 eV by scaling down the emission spectrum of the falling transition such that it matched the emission spectrum of the rising transition. Most importantly, the difference between the scaled spectrum of the falling transition and the spectrum of the rising transition results in a spectrum that approximately matches the emission of the forward-biased body diode. The emission

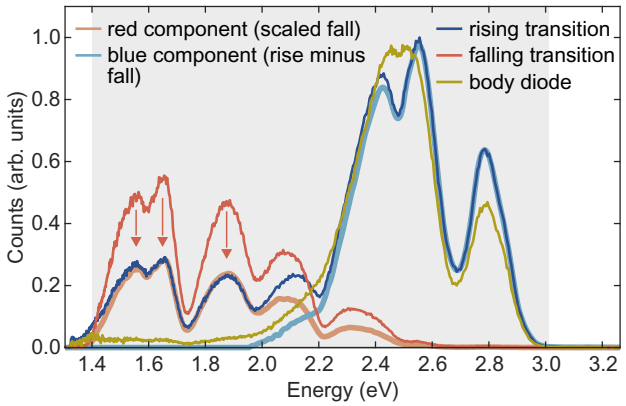

FIG. 3. Emission spectra from rising and falling V_{GS} transitions and from the forward-biased body diode. The emission spectrum of the rising transition (rise) is compared with the spectrum of the falling transition (fall). Scaling down the emission of the falling transition shows good agreement with the spectrum of the rising transition and is referred to as the "red component." The emission besides the red component at the rising transition is called the "blue component" and agrees with the emission of the body diode.

spectra of the body diode for a constant current, but differing V_{GS}, are shown in Fig. 4(a). Aside from the overall intensity, the spectrum does not depend on V_{GS}—we coherently obtained the same spectrum for each V_{GS} condition and consequently the same bulk recombination pathways at the body diode. The variation in the overall intensity can be explained by the variation in current through the diode, which decreases with increasing V_{GS} and the corresponding rise in current through the channel [see Fig. 4(b)]. This effect was previously used for condition monitoring [37,38].

The finding that the emission spectrum at the rising transition is rather blueish compared with the emission at the falling transition agrees with the finding of a previous study [29]. One of the most-important insights was that the emission spectrum of the falling transition is a subset of the emission spectrum of the rising transition. The spectra differ only by a scaling factor (see Fig. 3). Consequently, the recombination process for the falling transition equally occurs at the rising transition. Finally, the additionally observed emission at the rising transition is similarly present under a forward-bias condition of the body diode.

On the basis of their spectral location and associated human-perceived color (red 1.6–2.0 eV, blue 2.5–2.8 eV), we refer to the common spectral component of the rising and falling transitions as the "red component" and to the additional spectral component of the rising transition as the "blue component." Subsequently, we started a separate investigation of their behavior by modeling each spectrum as a superposition of these components (see Fig. 3).

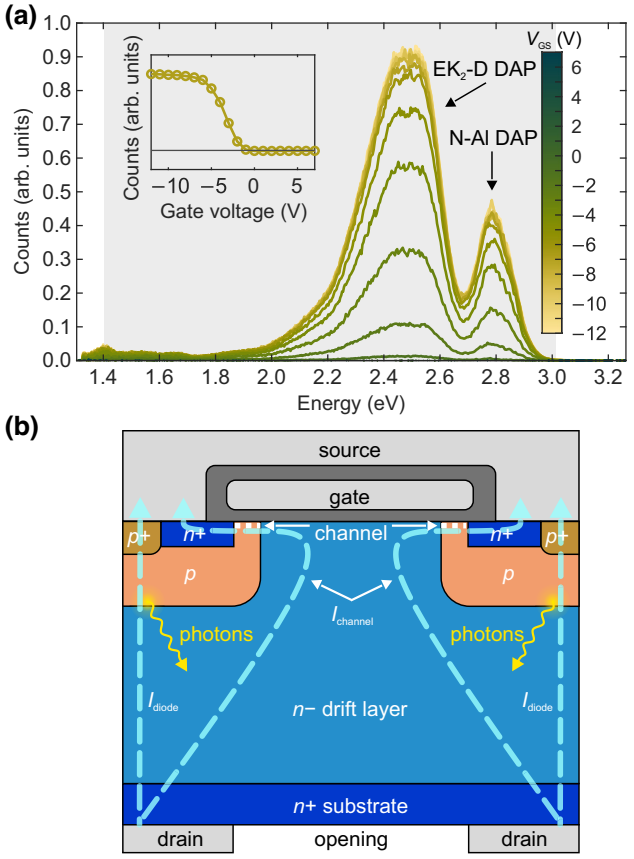

FIG. 4. Light emission from the forward-biased body diode. (a) Emission spectra obtained by applying a forward bias to the body diode at a constant current but differing V_{GS}. The inset shows the dependence of the integrated photon counts on V_{GS}. (b) The MOSFET cell and the currents flowing upon a forward biasing of the body diode.

A. The blue component

The fact that the additional emission spectrum occurring at the rising transition matches the emission spectrum of the body diode suggests that this blue component can be assigned to the same or similar types of 4*H*-SiC bulk defects, even though these emitting defects must be located at or close to the 4*H*-SiC/SiO_2 interface. As 4*H*-SiC bulk defects, including those occurring at *p*-*n* junctions, have been thoroughly investigated in the past, we can tentatively assign the peak at around 2.5 eV to DAP recombination between the so-called D center and a donor defect EK_2, which are both known from deep-level transient spectroscopy [39,40], with possibly further spectral contributions from $Z_{1,2}$ centers [41]. Furthermore, the peak at around 2.8 eV is assigned to DAP recombination between nitrogen and aluminum dopants [39,42]. Defect-assisted recombination involving the D_1 center could also contribute to this peak [32,43].

Although the blue component could potentially be assigned to DAP recombination on the basis of the literature mentioned [32,39–43], our experimental results hint at a donorlike defect close to the valence band and subsequent recombination with channel electrons [see Fig. 5(a)]. The discrepancy between the literature and our results could be related to extremely short trapping/detrapping time constants of the second defect state close to the conduction band, which would let the recombination appear to occur in direct interaction with the conduction band. This would explain why the blue component appears only at the rising transition and its dependence on the transition time (see Sec. VI).

Note that an inconspicuous portion of the blue component might be absorbed by the 4*H*-SiC substrate. On the basis of absorption measurements from a transition from nitrogen doping to a higher state in a previous study [34], we assume there is a Lorentzian-shaped absorption with a peak absorption coefficient $\alpha = \alpha_0 + \kappa c_n$, where $\kappa = 3.6 \times 10^{-17}\,\mathrm{cm}^2$, $\alpha_0 = 2.4\,\mathrm{cm}^{-1}$, and c_n is the *n*-type-nitrogen-doping concentration. Figure 5(a) shows the blue component, the normalized absorption peak, and the blue component corrected by the absorption of a substrate of 185 μm for several typical doping concentrations. It should be noted that the absorption peak coincides well with a valley in the emission spectrum.

B. The red component

Interestingly, most of the emission peaks of the red component are equally spaced in energy, which reminds one of phonon replicas of a single transition. As the energy spacing is about 220 meV—far higher than the energies of the highest phonon modes in 4*H*-SiC or SiO_2 of 120 and 137 meV, respectively—these replicas must be related to an LVM that can be modeled by a quantum mechanical harmonic oscillator [44]. The potential-energy surface of this harmonic oscillator is conventionally obtained from a one-dimensional harmonic approximation of the Born-Oppenheimer potentials involved. Introducing the potentials of two hypothetical states, 1 (ground state) and 2 (excited state), which are illustrated in Fig. 2(a), allowed us to consistently fit the emission spectrum of the red component. As discussed in detail in Appendix C, the emission spectrum, $I\left(E_{\mathrm{ph}}\right)$, of such a system, including broadening of transition energies, is given by

$$I\left(E_{\mathrm{ph}}\right) \propto \sum_{m,n} \omega_{\mathrm{ph}}^3 |\langle \phi_m^2 | \phi_n^1 \rangle|^2 L\left(E_{\mathrm{ph}}, E_{mn}, \sigma_{mn}\right), \qquad (1)$$

where ω_{ph} is the angular frequency of the emitted photon, $\langle \phi_m^2 | \phi_n^1 \rangle$ are the transition matrix elements, L is the line-shape function of the respective transition, E_{ph} is the energy of the emitted photon, and E_{mn} and σ_{mn} are the transition energy and its standard deviation, respectively.

Consequently, $I\left(E_{\mathrm{ph}}\right)$ is determined by four parameters (ΔE_{21}, $\hbar\omega_1$, $\hbar\omega_2$, Δq) describing the two harmonic potentials and four parameters (σ_1, σ_2, $\sigma_{\Delta E}$, ΔE_{L}) describing

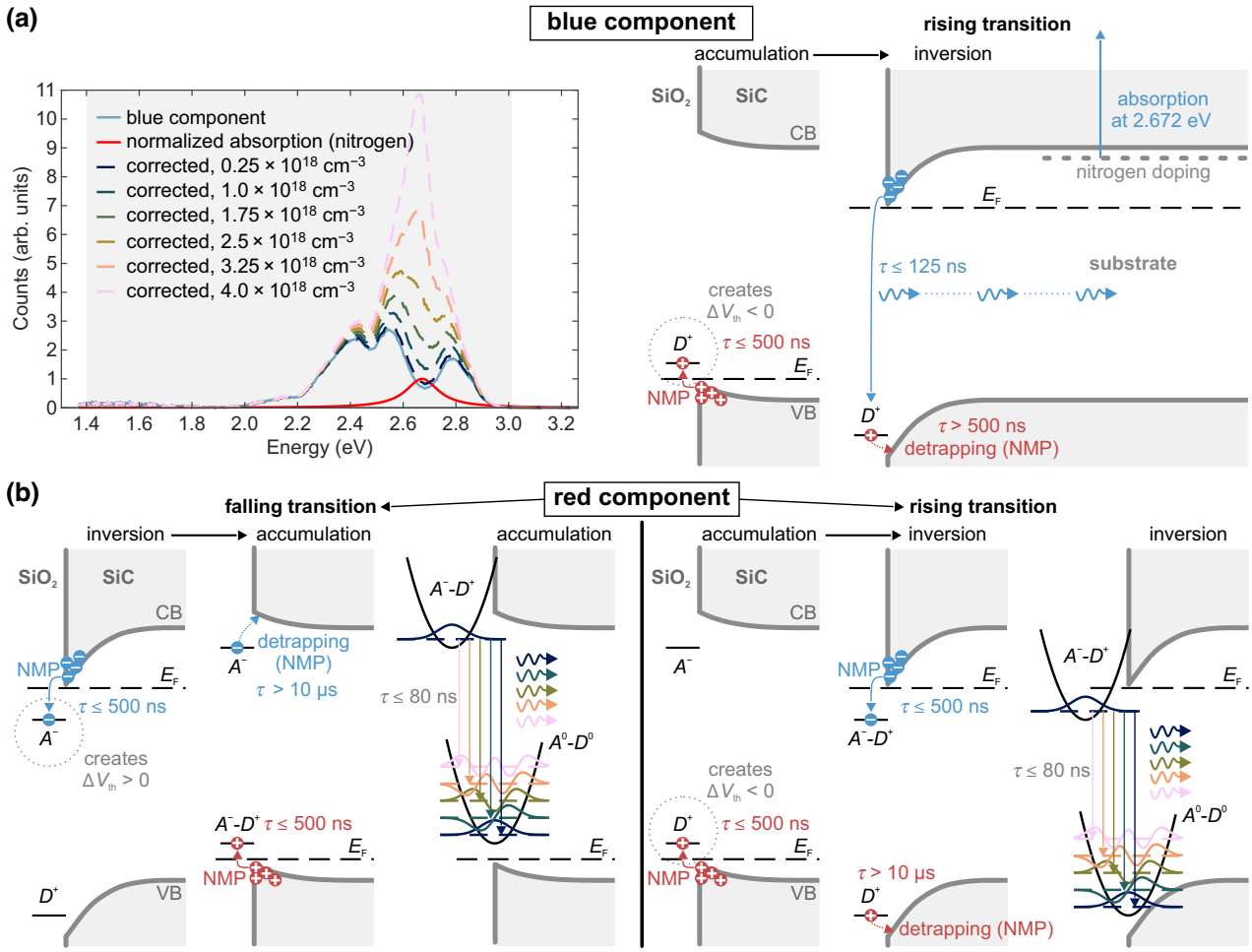

FIG. 5. Radiative transitions via interfacial point defects that constitute the red and blue components. (a) A portion of the blue component is probably absorbed by a transition from the nitrogen doping to a higher state in the conduction band. The impact of the absorption was calculated and plotted for different doping concentrations. According to the literature, the blue component can be mostly assigned to DAP recombination between a D center and an EK_2 center and nitrogen and aluminum dopants. However, in the experiments presented here, the blue component behaves more like a donorlike defect close to the valence band. Estimates for the range of time constants belonging to the different processes are indicated by τ and were obtained by the experiments performed. (b) The red component occurs at the rising and falling V_{GS} transitions and consists of multiple transitions from the vibrational ground state of electronic state 2 (A^--D^+) to the lowest five vibrational states of electronic state 1 (A^0-D^0). Before recombination, both an electron and a hole need to be trapped in the respective defect state. CB, conduction band; VB, valence band.

the broadening effects of the emission peaks. Typically, it is assumed that $\omega := \omega_1 = \omega_2$ and $\sigma := \sigma_1 = \sigma_2$, which reduced the total number of parameters from eight to six.

As shown in Fig. 2(a), fitting of this model to the emission spectrum of the falling transition for energies above 1.77 eV produces excellent agreement. The parameters and their values are listed in Table I. We obtained a ZPL of 2.53 eV and the emission lines were separated by $\hbar\omega = 220$ meV. As given by Eq. (C16), the value obtained for Δq translates into a Huang-Rhys factor of $S = 4.83$. The standard deviation σ of $\hbar\omega$ and the full width at half maximum (FWHM) of the Lorentz line shape ΔE_L were very small or even negligible. Consequently, broadening of the emission peaks is predominantly caused by the distribution of the charge transition levels, resulting in a Gaussian-distributed ΔE_{21} with a FWHM of $2\sqrt{2\ln(2)}\sigma_{\Delta E} = 158$ meV. Assuming that the standard deviations of the two charge transition levels are equal, their FWHM would be 112 meV.

TABLE I. Defect parameters obtained from the fit shown in Fig. 2(a).

	ΔE_{21} (eV)	$\hbar\omega$ (meV)	Δq	σ (meV)	$\sigma_{\Delta E}$ (meV)	ΔE_L (meV)
Value	2.53	220	3.11	0	67	2.1

Remarkably, the model nicely predicts the fifth emission peak at around 1.65 eV, but fails to predict the peak at around 1.55 eV. This additional emission peak is indicated in Fig. 2(a) as the difference between the measured emission spectrum and the extrapolated model. We assigned this additional peak to another type of defect, which is probably the $EH_{6/7}$ center [32].

Unfortunately, the model does not provide information on the absolute position of states 1 and 2 within the band gap of 4*H*-SiC ($E_{gap} = 3.26\,eV$). If the two states were centered within the band gap, they would be $\left(E_{gap} - \Delta E_{21}\right)/2 = 0.36\,eV$ from the band edges. The fact that the red component appears both at the rising transition and at the falling transition leads to the conclusion that it must be related to DAP recombination. In the context of the red component, we defined a donor D as a defect that emits an electron irrespective of its charge state and an acceptor A as a defect that captures an electron irrespective of its charge state. This is illustrated in Fig. 5(b). Independent of the type of transition, the red component is created by a transition from state 2 (A^--D^+) to state 1 (A^0-D^0). Before this transition, the other transitions between valence and conduction bands and the states A^- (falling transition) and D^+ (rising transition) are NMP transitions, which are strongly bias dependent and allow the linking of the transient shift of V_{th} to the photon emission [30]. This can be observed in the dependence of the photon emission on the bias levels, which is investigated in the next section.

IV. BIAS LEVELS

DAP recombination via the defect states discussed inherently involves trapping and detrapping of electrons and holes during the application of V_H or V_L, respectively. It is therefore expected that the properties of the prominent transient V_{th} shift will be reflected in the properties of the light emission. We have already observed such correlations for both stress and recovery in previous studies [30,31]. The setting considered here is similar to charge-pumping experiments [45,46], where the measured recombination current is analogous to the measured photon flux. However, it should be noted that every recombination pathway that contributes to a charge-pumping current will not necessarily involve a radiative transition that can be detected by optical spectroscopy.

In this section, we investigate how the red and blue spectral components depend on the gate bias levels, V_H and V_L. Analogously to the constant-V_L technique in charge-pumping experiments, we kept $V_L = -20\,V$ constant in deep accumulation, successively increased V_H, and measured the emission spectrum separately at the rising and falling V_{GS} transitions. Besides that, we kept $V_H = 20\,V$ constant in deep inversion and successively decreased the low level, which is the analogue of the constant-V_H technique in charge-pumping experiments. In total, we obtained four sets of spectra, which are shown in Figs. 6(a)–6(d). As mentioned in Sec. III, we can decompose each spectrum at the rising transition and determine the amplitudes of the red and blue components by fitting them to the measured spectrum. Hence, only two fitting parameters representing the amplitudes of the components are needed. Integration of the spectral components yields the associated total number of photon counts, which is shown for the rising and falling transitions in Figs. 6(e) and 6(f).

Along with optical spectroscopy, we used impedance spectroscopy to analyze the *C*-*V* characteristic of the tested MOSFET. This characteristic is well correlated with the optical emission intensity shown in Figs. 6(e) and 6(f). A significant increase in light intensity was observed for each component when the device entered inversion or accumulation. While the red component at the rising transition showed a rather V_{GS}-independent behavior, the blue component increased significantly with either decreasing or increasing bias. For the falling transition, the red component increased with increasing V_H and saturated or even decreased with decreasing V_L.

We also performed ultrafast V_{th} measurements to compare the light emission with the short-term charge-trapping behavior. For this purpose, we used a pristine device with intact drain metallization. Then we measured V_{th} at the end of the V_L or V_H phase before the respective V_{GS} transition after 4.1 ms of 500-kHz switching between 20 and −20 V with a transition time of 50 ns. The measurement delay time was set to 1 μs. Following our approach in Ref. [30] for double pulses, we fit the threshold-voltage data to the integrated photon counts as per

$$N_{int} = C_s |V_{th}\,(V_{GS}) - V_{0,s}|,\ s \in \{+,-\}, \tag{2}$$

where $V_{0,s}$ and C_s are fitting parameters for the rising (+) and falling (−) transitions, respectively. Despite some differences that probably arose from extensive, continuous switching, we found good agreement between the V_{th} measurement and the integrated photon counts.

In summary, the device exhibited light emission only upon switching between inversion and accumulation. This was observed by the strong increase in photon counts around the threshold and flat-band voltages that were determined by the *C*-*V* characteristic. Finally, the sum of all components correlated with the threshold voltage measured before the respective V_{GS} transition. Considering that V_{th} is directly related to the amount of trapped charge and the absence of spectral changes within the components themselves, the observations agree with the mechanisms illustrated in Fig. 5.

V. FREQUENCY AND DUTY CYCLE

Besides the bias levels, we also varied the switching frequency in the range from 20 to 1000 kHz for a fixed

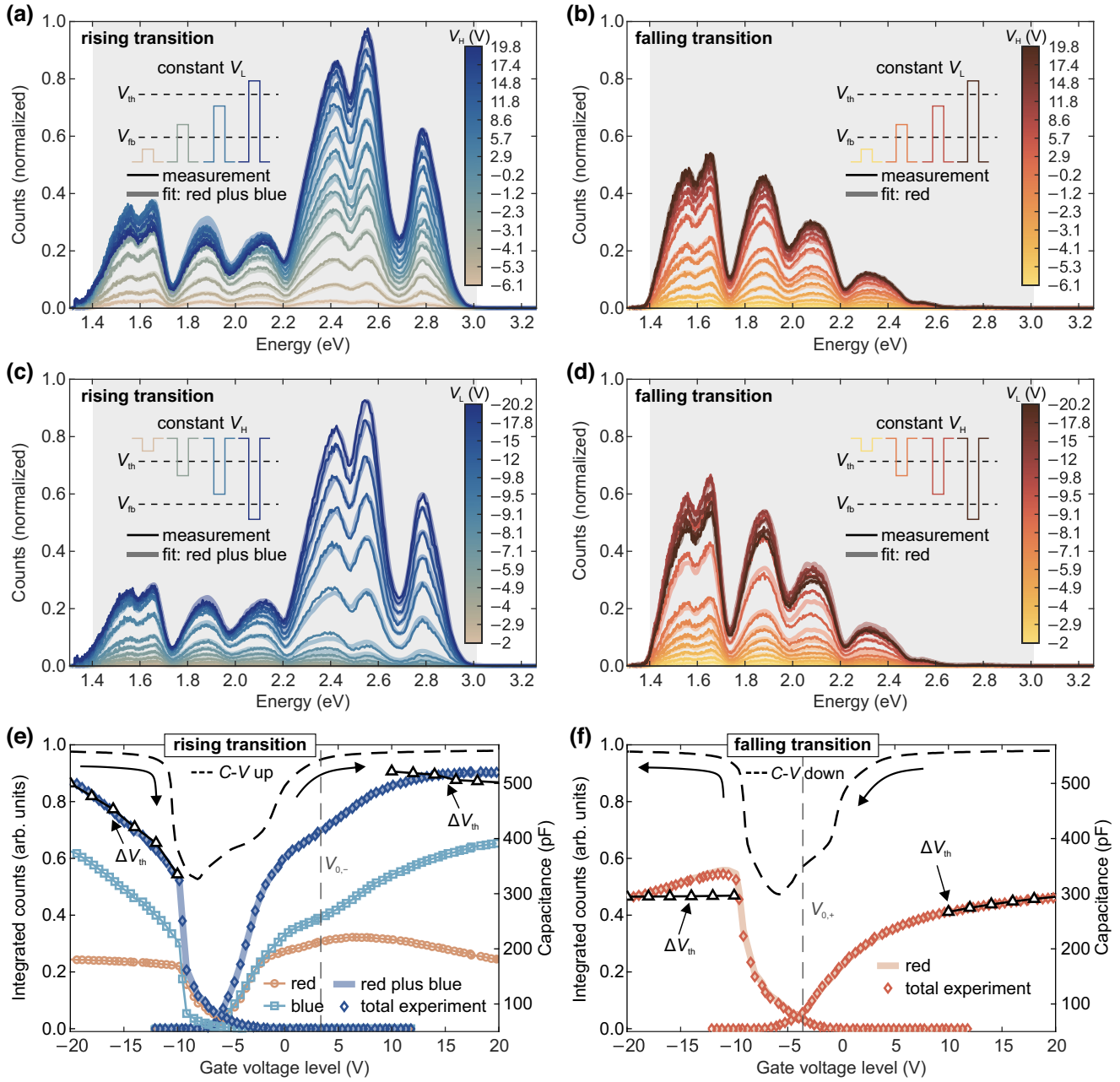

FIG. 6. Bias-level dependence. (a),(b) Emission spectra of the rising and falling transitions, respectively, while V_L is kept constant. (c),(d) Emission spectra of the rising and falling transitions, respectively, while V_H is kept constant. (e),(f) Integrated photon counts of the emission spectra at the rising and falling transitions, respectively, including constant-V_L and constant-V_H curves and their decomposition into the red and blue components. The corresponding up and down sweeps of the C-V characteristic and the fits based on Eq. (2) are shown as well.

duty cycle of 50% and the duty cycle in the range from 5% to 95% for a fixed frequency of 100 kHz. In these experiments, all spectra consisted of 2×10^6 V_{GS} transitions and the bias levels were set to 15 V/ − 15 V. The results are shown in Fig. 7. Despite small changes at around 1.6 eV in the emission spectrum of the falling transition [see Fig. 7(a)], we did not find any significant impact of either frequency or duty cycle. Therefore, the initial trapping of the later recombining charge carriers occurs very fast. At the bias levels used, the corresponding capture time constants needed to be well below 500 ns.

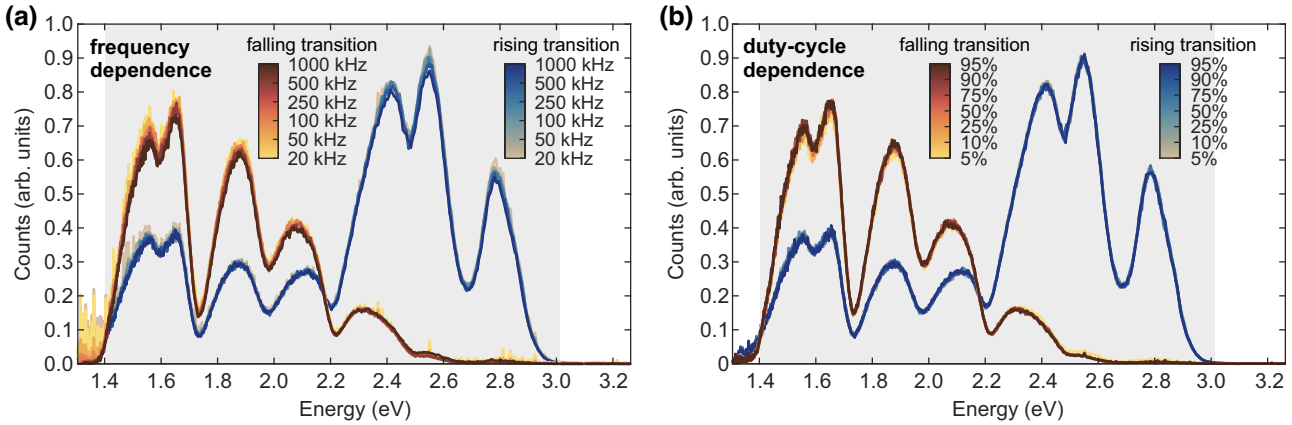

FIG. 7. Frequency and duty-cycle independence. (a) Frequency dependence of the emission spectra at the rising and falling transitions. (b) Duty-cycle dependence of the emission spectra at the rising and falling transitions.

VI. TRANSITION TIMES

In charge-pumping experiments, the recombination current typically decreases with increasing transition time. This is caused by detrapping of previously trapped charge carriers during the gate-voltage transition from inversion to accumulation or vice versa. Hereby, the charge-pumping current typically exhibits a linear relationship to the logarithm of the transition time [45].

Analogously, we investigated the light emission at the rising and falling transitions separately while varying either the rise time or the fall time. For this purpose, we used a 20 V/−20 V, 50-kHz gate waveform and separately varied the transition times from 0.5 µs up to 8 µs, while keeping the other transition time constant at 0.5 µs. Analogously to the investigation of the bias-level dependence, discussed in Sec. IV, we extracted the red and blue components from the emission spectra of the rising transition to determine their respective dependency.

The results are shown in Fig. 8. We found for all spectral components the same linear relation to the logarithm of the transition time. First, the emission spectrum at the rising transition was not affected by the fall time and the emission spectrum at the falling transition was not affected by the rise time. Second, although the long-term limit is certainly decreasing light emission with increasing transition time, we found, in the investigated regime of transition times, an increasing red component with both an increasing rise time at the rising transition and an increasing fall time at the falling transition. In contrast, the blue component at the rising transition decreases with increasing rise time, as typically observed for the recombination current through interface defect states in charge-pumping experiments.

The independence of radiative recombination at the falling transition from the rise time and at the rising transition from the fall time agrees with the postulated short capture time constants from Sec. V. The decreasing blue component with increasing rise time at the rising transition rather agrees with a donorlike state close to the valence band (see Fig. 5). The increasing red component with increasing rise time at the rising transition and with increasing fall time at the falling transition is related to a peculiarity of DAP recombination. In contrast to the recombination between a defect state at the interface and either the valence band or the conduction band, which is the basic assumption in charge-pumping experiments, both the donor state and the acceptor state have to first capture and sustain a charge carrier so that recombination between them can occur. Consequently, depending on the time constants involved, there is a regime of increasing recombination with increasing transition time. This is discussed in greater detail in Sec. VIII C.

VII. TEMPORAL RESOLUTION

As mentioned in Sec. II, the ICCD camera used features a minimum t_{gate} of 3 ns. Apparently, this not only allows the detection of the temporal evolution of the emission spectrum over an entire gate-voltage period but also resolves the temporal evolution during the V_{GS} transition itself.

For this experiment, we used a frequency of 78.1 kHz, corresponding to a period of 1.28 µs, with voltage levels of 15 V/ − 15 V and a transition time of 50 ns. We used the mentioned minimum gate width of 3 ns. Again, we extracted red and blue components from each spectrum. Figure 9(a) shows the raw data of the entire experiment and Fig. 9(b) presents the corresponding fitted dataset, consisting of a superposition of red and blue components. Each spectrum was fitted independently. For two exemplary spectra, the quality of the fit is shown in Fig. 10(a). The two components from Fig. 3 nicely reproduced the observed spectra. Subsequently, we investigated the red and blue components separately. The amplitudes

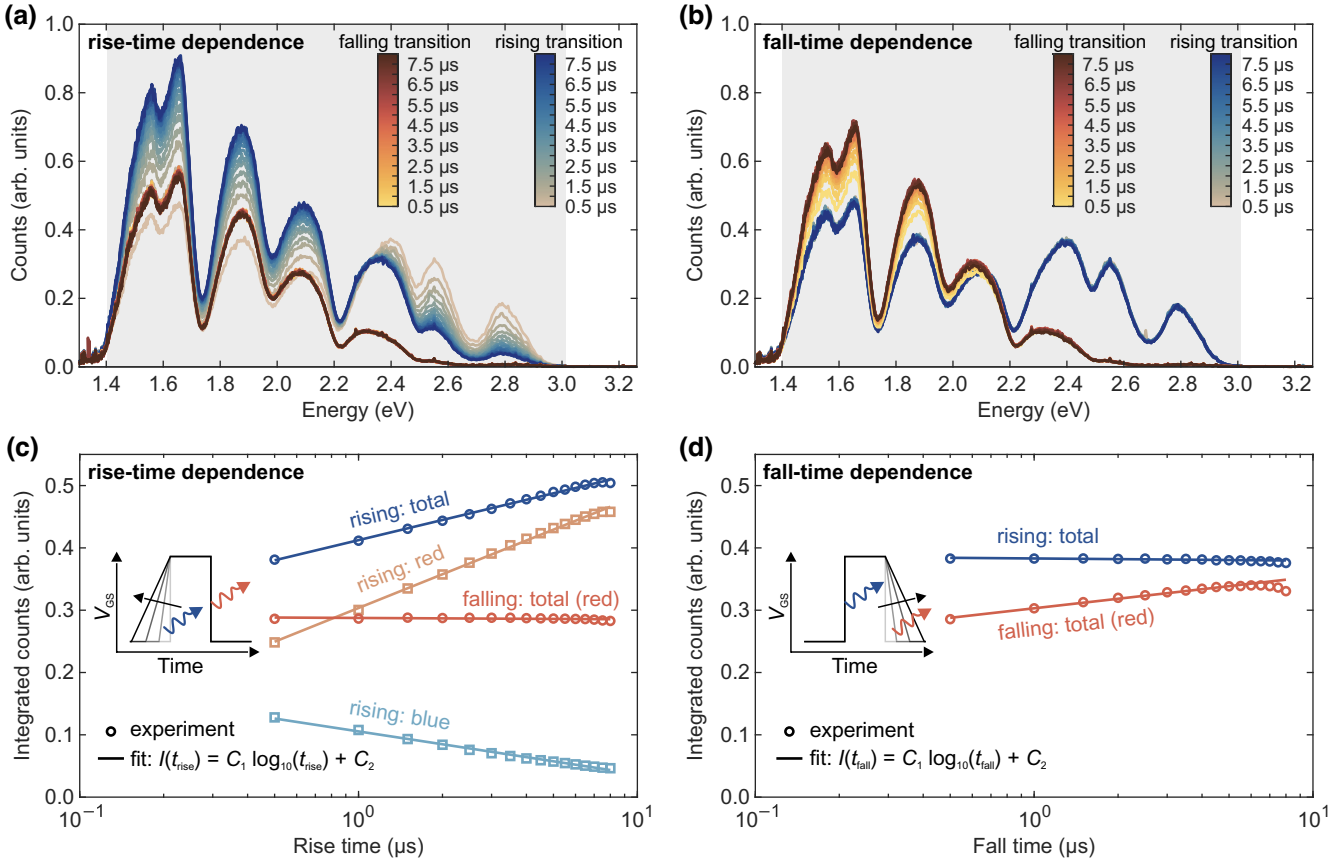

FIG. 8. Transition-time dependence. (a) Rise-time dependence and (b) fall-time dependence of the emission spectra at the rising and falling transitions. (c) Rise-time dependence and (d) fall-time dependence of the integrated photon counts of the total emission spectrum and the red and blue components.

of the spectral components are plotted with a linear y axis in Fig. 10(b) and with a logarithmic y axis in Fig. 10(c).

As already found in our previous work [30,31], the light emission is on a linear scale strongly localized at the switching transitions. On a logarithmic scale, shown in Fig. 10(c), all three decay curves show a biexponential decay. Consequently, the decay curves can be described by

$$I\left(t_{\mathrm{gate,del}}\right) = C \exp\left(-\frac{t_{\mathrm{gate,del}} - t_0}{\tau_1}\right) + (1 - C) \exp\left(-\frac{t_{\mathrm{gate,del}} - t_0}{\tau_2}\right). \quad (3)$$

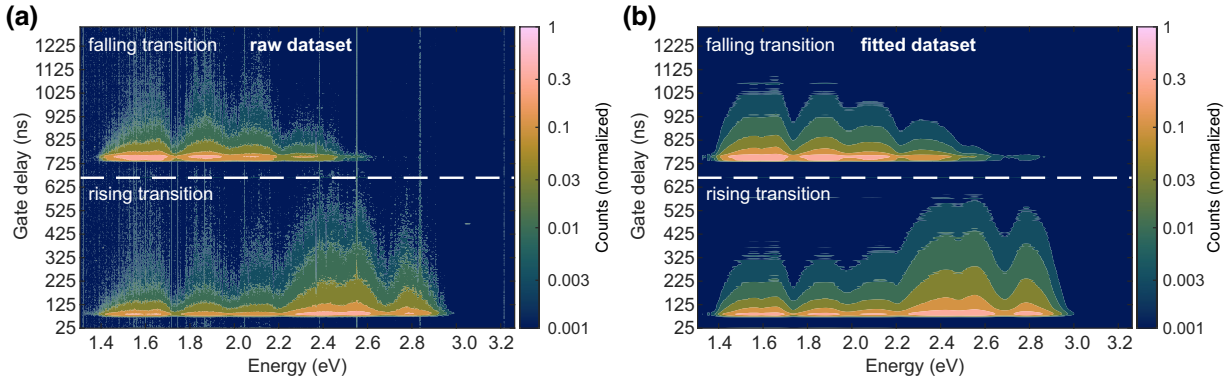

FIG. 9. Contour plot of time-resolved emission spectra over an entire gate-voltage period of 1280 ns. Each horizontal line corresponds to an emission spectrum for the respective gate delay indicated on the vertical axis. Each spectrum was measured within a gate time window of 3 ns. The gate delay time was successively increased to scan the entire gate-voltage period. (a) Normalized raw dataset. (b) Normalized dataset fitted with red and blue components.

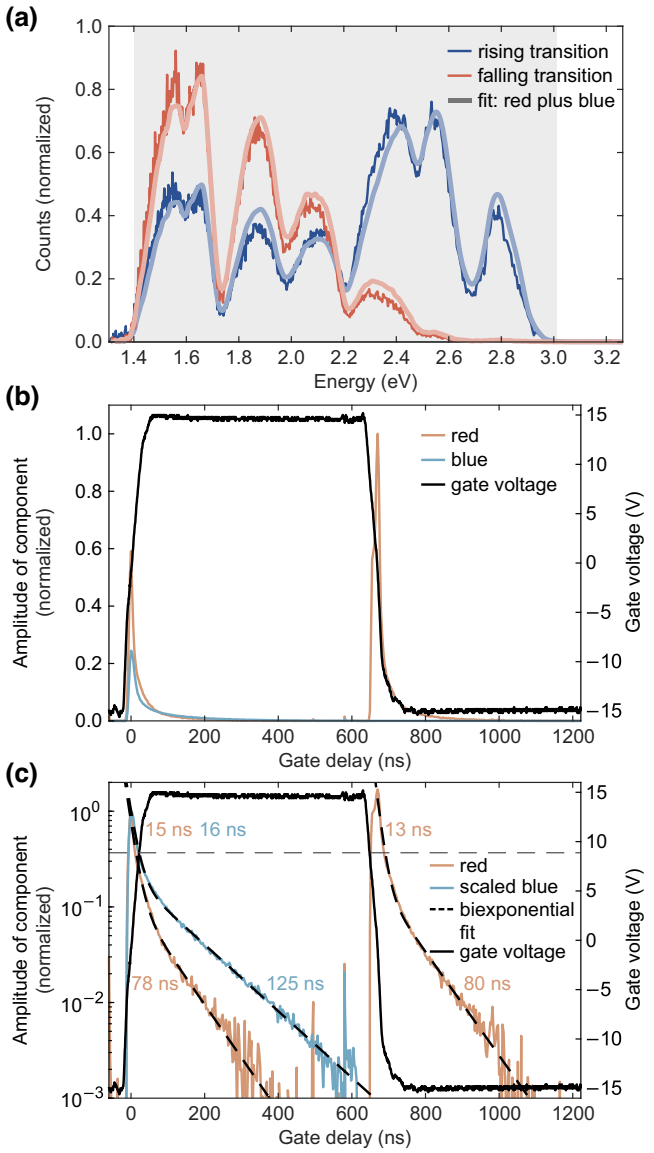

FIG. 10. Temporal evolution of the red and blue components over one gate-voltage period. (a) Exemplary fits of emission spectra from the total dataset shown in Fig. 9. (b) Temporal evolution of the two components on a linear y scale. (c) Temporal evolution of the two components on a logarithmic y scale.

For each normalized component, t_0 is the time of maximum photon emission. The parameter C represents the share of the first exponential decay, and τ_1 and τ_2 are the respective decay time constants. These parameters can be obtained by fitting and are listed in Table II.

Apparently, the red component exhibits the same τ and C for both transitions. As the decay with τ_1 overlaps in time with the gate voltage transitions themselves, the deduction of the underlying physical mechanism is rather complicated. However, the decay with τ_2 occurs during the phase of constant gate voltage. As the τ_2 values agree, we can conclude that the underlying recombination mechanism must be identical for both transitions. The blue component has about the same short decay time constant τ_1, but differs significantly in τ_2, which is almost 60% larger compared to that of the red component.

TABLE II. Parameter values obtained by fitting Eq. (3) to the data in Fig. 10(c).

	Red			Blue		
	C	τ_1 (ns)	τ_2 (ns)	C	τ_1 (ns)	τ_2 (ns)
Rising	0.87	15	78	0.80	16	125
Falling	0.89	13	80	...	...	...

The observation that the radiative-decay time constants are identical for the rising and falling transitions agrees with the proposal made in Sec. III—the red component stems from DAP recombination and associated vibrational sidebands. The reason for the higher τ_2 of the blue component is, as of now, not entirely clear. However, as the red components agree, it confirms our understanding of splitting the total spectrum at the rising transition into the two components.

VIII. DISCUSSION

As discussed in the previous sections, the underlying defects belonging to the red and blue components are most probably very different. The idea presented in Sec. III, of decomposing all spectra into their respective components, was useful to study their individual properties. On the basis of the fitting of the red component arising at the falling transition of V_{GS}, we identified ΔE_{21}, $\hbar\omega$, and Δq as physical defect parameters that can be used to search for possible defect candidates that might be the origin of this component.

A. Carbon clusters as the cause of the red component

As shown in Sec. III, the observed emission spectra at the falling transition clearly exhibit the signature of radiative recombination between the vibrational ground state of an excited electronic state and vibrational sidebands of an electronic ground state. The spacing $\hbar\omega = 220$ meV of the vibrational sidebands is considerably greater than the energies of the highest optical phonon modes of about 120 and 137 meV in 4H-SiC and SiO_2, respectively [47–49]. Thus, the observed vibrational sidebands must stem from LVMs of the underlying defect, which can be higher in energy than collective lattice vibrations [44].

Indeed, several different LVMs with energies of up to 247 meV have been detected in 4H-SiC in low-temperature photoluminescence measurements [50,51]. These LVMs are exclusively linked to carbon clusters [52–55], whose emission intensity and ZPL depend on quantities such as doping concentration and annealing temperature [50,56]. Carbon clusters likely exist in a similar

fashion at the 4*H*-SiC/SiO_2 interface, and their density can be reduced with a phosphorus treatment [57]. Photoluminescence from interface defects, mostly at around 1.55–2.48 eV, not only exhibited LVMs of up to 220 meV, but could also successfully be linked to the interface-defect density extracted by capacitance-voltage measurements [58,59]. Note that the LVM and the energy range perfectly agree with the red component. Most probably the same defects were shown to be single-photon emitters, whereby their polarization hints at defects at the SiC side of the interface [60–62]. It was speculated that the observed single-photon emitters were carbon- or oxygen-related interface defects, as they appeared after thermal oxidation of the SiC surface and disappeared again after the oxide was removed. Two-dimensional mapping of these defects was performed with use of confocal photoluminescence and tunneling electroluminescence methods [63,64] as well as capacitive methods [65]. In all cases, the observed defects predominantly appeared at the bumps on the (0001) crystal surface.

As mentioned earlier, the fact that the red component, which is suspected to originate from carbon clusters, appears at the falling and the rising transitions leads to the conclusion that the underlying process requires the trapping of both an electron and a hole in acceptor (A^-) and donor (D^+) states first, before the actual recombination event occurs [Fig. 5(b)]. Otherwise, the band electrons or holes would rapidly disappear during the switching event, such that no recombination event would occur. These donor and acceptor states bind the respective charge carrier long enough for the opposite charge carrier to also get trapped, so that they can subsequently recombine.

From comparison of our observed LVM with theoretical and experimental results from the literature for bulk 4*H*-SiC, it might be suspected that the observed LVM stems either from cubic and/or hexagonal tricarbon antisite clusters [$(C_3)_{Si,k}$ and $(C_3)_{Si,h}$] or from cubic and/or hexagonal tetracarbon interstitials [$(C_{BC})_{4,kkkk}$ and $(C_{BC})_{4,hhhh}$] [51,52,54], which show similar values for ZPL, $\hbar\omega$, and the Huang-Rhys factor (see Table III) [54]. Differences might originate from changes in stiffness of the environment around the clusters at the interface. Furthermore, the presented theoretical values consider only direct transitions of bound excitons that involve a donor state. As the experimentally observed emission peaks are symmetric, excluding significant Coulomb interaction, the DAP transition cannot be related to a typical pair of defects, but must be related to a single complex. Because of the clear signature of the LVM, we therefore concluded that the known carbon clusters probably serve as building blocks of such a defect complex that features the observed DAP transition. Note that such a carbon-cluster complex has not been investigated so far by density-functional-theory calculations.

TABLE III. Comparison between defect parameters obtained by experiment and theoretically calculated values from the literature [54].

Parameter	Expt.	$(C_3)_{Si,k}$	$(C_3)_{Si,h}$	$(C_{BC})_{4,kkkk}$	$(C_{BC})_{4,hhhh}$
ZPL (eV)	2.53	2.56	2.67	2.36	2.49
$\hbar\omega$ (meV)	220	249	247	193	192
S	4.83	2.59	2.35	5.1	5.5

B. Relation between threshold-voltage shift and light emission

Apparently, the blue and red components are both the result of recombination, before which a transient shift in V_{th} is created (see Fig. 5). As shown in previous studies [30,31] and also here in Sec. IV, there is a clear correlation between the transient V_{th} shift and light emission for both positive and negative bias. Charging and discharging of the involved donor and acceptor states creates this correlation (see Fig. 5).

Rising transition: Before a recombination event, the negative bias during the V_L phase leads to trapping of holes in the donor state, D, close to the edge of the valence band. This leads to a decreased V_{th}.

Falling transition: Before a DAP recombination event, the positive bias during the V_H phase leads to trapping of electrons in the acceptor state, A, close to the edge of the conduction band. This leads to an increased V_{th}.

We stipulate that this is the reason for the bias-level dependence, as observed in Fig. 6, and the relation between V_{th} and the light emission following Eq. (2). The more the donor or acceptor states get charged during the V_L and V_H phases, respectively, the more the charges undergo recombination and the higher the absolute V_{th} shift before the switching event.

C. Competing DAP recombination and nonradiative detrapping

One interesting observation was that the red component increased at the rising transition with increasing rise time and at the falling transition with increasing fall time. In charge-pumping experiments, the recombination current usually decreases with increasing transition time [45,46], which was observed for the blue component. However, as the process of recombination depends on both donor and acceptor states, the red component can also increase with the transition time. Let us consider the falling transition as an example: During the transition, previously trapped electrons can be nonradiatively detrapped from the acceptor state back to the conduction band via an NMP process (see Fig. 5). Moreover, the holes must be trapped in the donor state close to the valence band before DAP recombination. Depending on the time constants of the trapping

and detrapping processes, which are strongly bias dependent, either increasing or decreasing DAP recombination with increasing transition time can be observed.

IX. CONCLUSION

In our study, we conducted time-gated spectral detection of light emission through the back side of a fully processed SiC power MOSFET with remaining metal drain contact during gate switching. Our findings revealed the existence of two spectral components that constituted the emission spectrum and that we referred to as the red and blue components.

On the basis of fitting the red component with a quantum mechanical model, we identified the red component as a DAP recombination process involving an LVM of 220 meV, characterized by a ZPL and four LVM sidebands. Such a highly energetic LVM, well above the highest phonon modes in $4H$-SiC and SiO_2, is in general extremely rare, which allowed us to assign the red component to a carbon-cluster-like defect complex at the $4H$-SiC/SiO_2 interface.

The blue component could stem from two different DAP recombination pathways. The first pathway is between the D center and an EK_2 center, and the second is between nitrogen and aluminum dopants. These pathways could be identified by comparing the blue component with the emission spectrum of the body diode, which has been more-thoroughly studied in the literature. However, in our experiments, the blue component behaved rather like a recombination between a donorlike defect close to the valence band and channel electrons.

We were also able to link the bias-level dependence of the spectral components to the transient V_{th} shift and the C-V characteristic that confirms the understanding of the two components. Furthermore, we observed an independence of the emission spectra on switching frequency (20–1000 kHz) and duty cycle (5%–95% at 100 kHz), revealing extremely fast trapping processes with time constants below 500 ns in strong inversion or accumulation.

In addition, we successfully traced the changes in the spectral components during a V_{GS} period and analyzed the effects of differing transition times. The results further confirmed the understanding of the two components and we found a linear dependence on the logarithm of the transition time, as observed for recombination current in charge-pumping experiments.

Overall, our method of time-gated optical spectroscopy through the back side of a fully processed SiC MOSFET opens new avenues for characterizing and identifying interface states and related recombination processes. This method of characterizing interface states paves the way for further research on improving the reliability and performance of these devices.

ACKNOWLEDGMENTS

Financial support by the Austrian Federal Ministry for Digital and Economic Affairs, the National Foundation for Research, Technology and Development, and the Christian Doppler Research Association is gratefully acknowledged.

APPENDIX A: WAVELENGTH AND INTENSITY CALIBRATION

To understand and model the light emission from a SiC MOSFET, calibration of the measurement system consisting of the spectrograph and the ICCD is important. Also, as the investigated light emission covers the entire range of visible light, intensity and wavelength calibration are of particular importance. If either of the two is not performed, it can have a strong impact on both the shape and the energetic position of the emission peaks. For our experiments, each spectroscopic measurement was performed with a background correction of the CCD. Both calibrations were performed with the IntelliCal system from Teledyne Princeton Instruments.

For wavelength calibration, we used a neon-argon light source and achieved a calibration in the range from 585 to 966 nm with an root-mean-square of 0.2 nm. We also validated the calibration using a mercury lamp with emission lines in the range from 254 to 579 nm [see Fig. 11(a)] to confirm the calibration for shorter wavelengths. For intensity calibration, we used a set of temperature-compensated, light-emitting diodes (LEDs) that provide the spectrum as shown in Fig. 11(b) measured at the U.S. National Institute of Standards and Technology. Using IntelliCal, we accordingly performed an intensity calibration and extracted the correction factor, F_{corr}, that links the calibrated and noncalibrated spectra via

$$I_{cal}(\lambda) = F_{corr}(\lambda)\, I_{raw}(\lambda)\,. \tag{A1}$$

Subsequently, we determined a wavelength range where we could particularly trust our measured spectra. This range was defined such that the measured noncalibrated intensity in each pixel, normalized to the maximum at 746 nm, was above 10^{-2}. The trusted wavelength range located between 412 and 884 nm is indicated by a gray background. Outside the trusted wavelength range, we set F_{corr} to the last value of a smoothed (local regression with a second-degree polynomial and weighted linear least squares) within the trusted wavelength region such that F_{corr} becomes constant [see Fig. 11(c)]. Note that the set of LEDs provided light emission in the nontrusted region above 884 nm. However, as the quantum efficiency of the built-in intensifier in the ICCD strongly drops in this region, this yields a steeply increasing correction factor. The light is simply not detected. For the nontrusted region below 412 nm, however, there is no light from the LEDs, which is why the correction factor approaches zero

although the quantum efficiency is still significant [confirmed by the detection of mercury lines at 405 and 436 nm, as shown in Fig. 11(a)]. Therefore, if there was light emission below 412 nm, we would still see the light in the raw data but not in the calibrated data. In summary, this is the reason behind defining trusted and nontrusted regions. By setting the correction factor as constant in the nontrusted regions, instead of setting it as zero, we could still observe whether we detected light in the region below 412 nm.

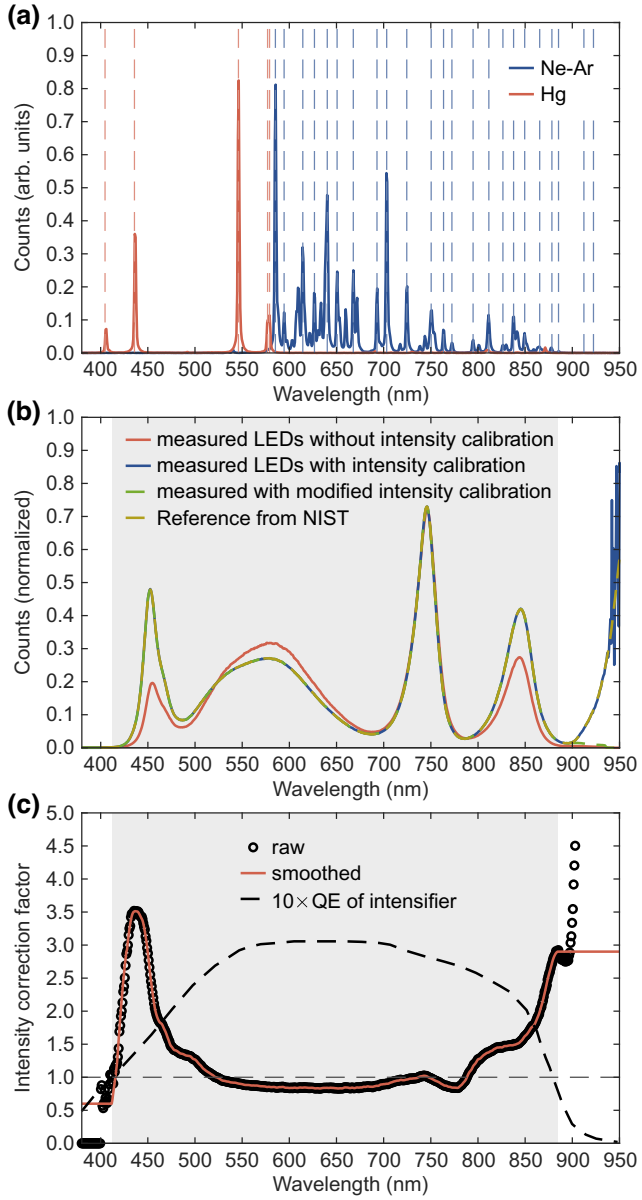

FIG. 11. Intensity and wavelength calibration of spectrograph and ICCD. (a) Emission spectra of mercury (Hg) and neon-argon (Ne-Ar) lamps measured with the wavelength-calibrated setup. The vertical line indicates the true position of the respective peak. (b) Spectra involved in intensity calibration. (c) Correction factor for intensity calibration. It is not exclusively determined by the quantum efficiency (QE) of the intensifier, but it rather reflects the efficiencies of all optical components along the light path between the entrance slit of the spectrograph and the CCD. NIST, National Institute of Standards and Technology.

APPENDIX B: OPEN VERSUS PARTIALLY GROUNDED DRAIN CONTACT

There was a change in the device characteristic when the drain contact was partially removed, which is shown in Fig. 12(a). However, this difference vanished almost completely when the drain terminal was kept floating, as shown in Fig. 12(b). The bias dependence of the emission spectra, shown in Figs. 6(e) and 6(f), reflects this behavior.

APPENDIX C: MODEL FOR THE RED COMPONENT

To determine the transition rate, k_{mn}, from the vibrational level, m, of electronic state 2 to the vibrational level, n, of state 1 [see Fig. 2(a)], Fermi's golden rule

$$k_{mn} = \frac{2\pi}{\hbar} |\langle \Psi_m^2 | \hat{\mu} | \Psi_n^1 \rangle|^2 \delta \left(E_m^2 - E_n^1 - \hbar\omega_{\mathrm{ph}} \right) \qquad \text{(C1)}$$

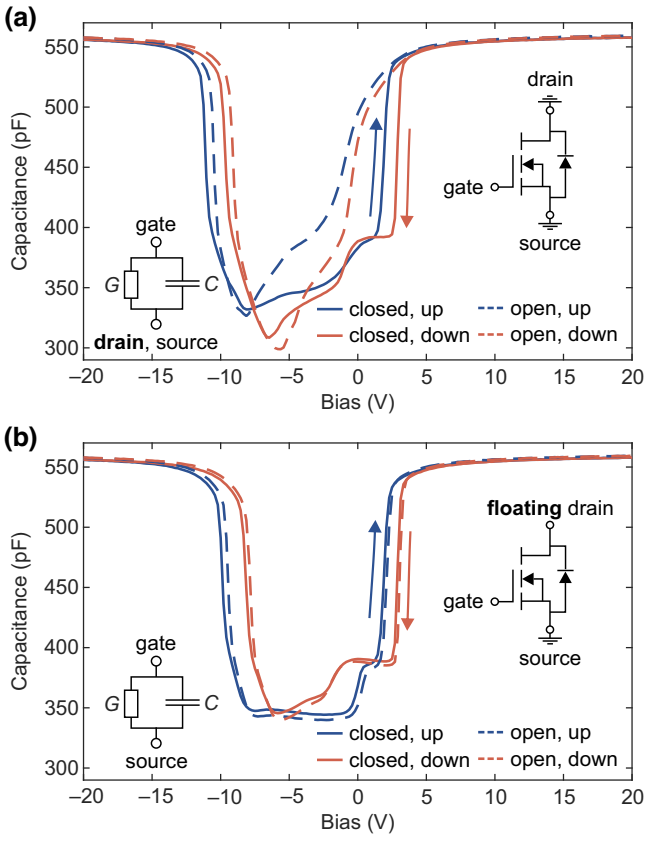

FIG. 12. *C-V* curves of pristine devices and devices that were opened from the back side. (a) *C-V* curves of a pristine (closed) device and an opened device with grounded drain terminals. (b) *C-V* curves of a pristine (closed) device and an opened device with floating drain terminals.

is used. It is a consequence of time-dependent perturbation theory. Here, $\hat{\mu}$ is the perturbation operator, which in the case of photon emission is the dipole operator.

With use of the Born-Oppenheimer approximation [66], the total wave function can be expressed as a product of the electronic wave function ψ, the rotational wave function Φ, and the vibrational wave function ϕ:

$$\Psi_n^i = \underbrace{\psi^i}_{\text{electronic}} \underbrace{\Phi^i \phi_n^i}_{\text{nuclear}}. \tag{C2}$$

The dipole operator is assumed to be independent of the nuclear coordinates, which allows us to consider only the vibrational component (Franck-Condon factor). Additionally, a factor of ω_{ph}^3 enters the equation [67]:

$$k_{mn} \propto \omega_{\text{ph}}^3 |\langle \phi_m^2 | \phi_n^1 \rangle|^2 \delta \left(E_m^2 - E_n^1 - \hbar\omega_{\text{ph}} \right). \tag{C3}$$

For each of the two states, we approximated the Born-Oppenheimer surfaces by harmonic potentials in one dimension, leading to the well-known Schrödinger equation

$$-\frac{\hbar^2}{2m_i}\frac{\mathrm{d}^2}{\mathrm{d}x^2}\phi_n^i(x) + \frac{1}{2}m_i\omega_i^2 x^2 \phi_n^i(x) = E_n^i \phi_n^i(x), \tag{C4}$$

which has to be solved for each of the two states. Depending on the energy range considered, a description based solely on a harmonic potential may not always be sufficient, because the underlying Born-Oppenheimer potential could be anharmonic [68], which leads to a gradually decreasing spacing in the vibrational energy levels with increasing energy. This could be modeled by replacement of the harmonic potential by the Morse potential [44,69]. However, as we observed equally spaced emission peaks within the spectral range considered, the harmonic potential was fully sufficient. With the coordinate transformation

$$x \to q = \sqrt{\frac{m_i\omega_i}{\hbar}}x \tag{C5}$$

the Schrödinger equation simplifies to

$$-\frac{1}{2}\hbar\omega_i\frac{\mathrm{d}^2}{\mathrm{d}q^2}\phi_n^i(q) + \frac{1}{2}\hbar\omega_i q^2 \phi_n^i(x) = E_n^i \phi_n^i(q), \tag{C6}$$

whereby the potential translates to

$$V(q) = \frac{1}{2}\hbar\omega_i q^2. \tag{C7}$$

The solution of the Schrödinger equation of the harmonic oscillator can be found in any textbook on basic quantum mechanics. Here, the vibrational eigenstates ϕ_n^i of electronic state $i \in \{1,2\}$, numbered by index $n \in \{0,1,2,3,\ldots\}$, are given by

$$\phi_n^i(q) = \frac{1}{(2^n n!)}\left(\frac{1}{\pi}\right)^{1/4} \exp\left(-\frac{q^2}{2}\right) H_n(q), \tag{C8}$$

with H_n being the nth Hermite polynomial. Furthermore, the energy eigenvalues E_n^i are given by

$$E_n^i = \hbar\omega_i\left(\frac{1}{2} + n\right). \tag{C9}$$

Consequently, $\hbar\omega$ is the distance between the energy levels and scales with the curvature of the harmonic potential. The potentials of states 1 and 2 are separated by Δq and ΔE_{21}.

In the most-general case, the pure underlying lifetime-limited line shape is a Lorentzian following

$$f\left(E_{\text{ph}}, E_{mn}, \Delta E_{\text{L}}\right) = \frac{\Delta E_{\text{L}}/2\pi}{\left(E_{\text{ph}} - E_{mn}\right)^2 + \left(\Delta E_{\text{L}}/2\right)^2}. \tag{C10}$$

Broadening of this line shape was introduced by the assumption of a Gaussian distribution in ω_1, ω_2, and ΔE_{21}. As convolution operations follow commutativity and associativity and a convolution of two Gaussians yields another Gaussian with a modified width, we can compute the final line shape as a convolution of the Lorentzian and a Gaussian:

$$L\left(E_{\text{ph}}, E_{mn}, \sigma_{mn}, \Delta E_{\text{L}}\right) = \int_{-\infty}^{\infty} G\left(E', \sigma_{mn}\right) f\left(E_{\text{ph}} - E', E_{mn}, \Delta E_{\text{L}}\right) \mathrm{d}E', \tag{C11}$$

where the width of the Gaussian is given by

$$\sigma_{mn} = \sqrt{\sigma_1(n)^2 + \sigma_2(m)^2 + \sigma_{\Delta E}^2} \tag{C12}$$

with standard deviations

$$\sigma_i(n) = \sigma_i\left(\frac{1}{2} + n\right) \tag{C13}$$

that depend on the vibrational quantum number because

$$E_{\text{ph}} = E_m^2 - E_n^1 + \Delta E_{21} \tag{C14}$$

$$= \hbar\omega_2\left(\frac{1}{2} + m\right) - \hbar\omega_1\left(\frac{1}{2} + n\right) + \Delta E_{21}. \tag{C15}$$

The line-shape function L finally replaced the Dirac δ distribution in Eq. (C3) and all transitions considered were summed up, which resulted in the emission spectrum presented in Eq. (1).

Finally, the Huang-Rhys factor S is defined as the number of vibrational quanta that are involved in the radiative transition. With use of the coordinate q as defined in Eq. (C5), it is therefore given by

$$S = \frac{1}{2}(\Delta q)^2 . \tag{C16}$$

[1] F. Roccaforte, P. Fiorenza, G. Greco, R. L. Nigro, F. Giannazzo, A. Patti, and M. Saggio, Challenges for energy efficient wide band gap semiconductor power devices, Phys. Status Solidi (a) **211**, 2063 (2014).

[2] J. Millan, P. Godignon, X. Perpina, A. Perez-Tomas, and J. Rebollo, A survey of wide bandgap power semiconductor devices, IEEE Trans. Power Electron. **29**, 2155 (2014).

[3] M. W. Geis, T. C. Wade, C. H. Wuorio, T. H. Fedynyshyn, B. Duncan, M. E. Plaut, J. O. Varghese, S. M. Warnock, S. A. Vitale, and M. A. Hollis, Progress toward diamond power field-effect transistors, Phys. Status Solidi (a) **215**, 1800681 (2018).

[4] B. Baliga, Power semiconductor device figure of merit for high-frequency applications, IEEE Electron Device Lett. **10**, 455 (1989).

[5] L. Zhang, X. Yuan, X. Wu, C. Shi, J. Zhang, and Y. Zhang, Performance evaluation of high-power SiC MOSFET modules in comparison to Si IGBT modules, IEEE Trans. Power Electron. **34**, 1181 (2019).

[6] B. Hull, S. Allen, Q. Zhang, D. Gajewski, V. Pala, J. Richmond, S. Ryu, M. O'Loughlin, E. V. Brunt, L. Cheng, A. Burk, J. Casady, D. Grider, and J. Palmour, in *2014 IEEE Workshop on Wide Bandgap Power Devices and Applications* (IEEE, Knoxville, TN, USA, 2014), p. 139.

[7] C. R. Eddy and D. K. Gaskill, Silicon carbide as a platform for power electronics, Science **324**, 1398 (2009).

[8] C. Langpoklakpam, A.-C. Liu, K.-H. Chu, L.-H. Hsu, W.-C. Lee, S.-C. Chen, C.-W. Sun, M.-H. Shih, K.-Y. Lee, and H.-C. Kuo, Review of silicon carbide processing for power MOSFET, Crystals **12**, 245 (2022).

[9] G. Rescher, G. Pobegen, T. Aichinger, and T. Grasser, in *2016 IEEE International Electron Devices Meeting (IEDM)* (IEEE, San Francisco, CA, USA, 2016), p. 1.

[10] H. Li, S. Dimitrijev, H. B. Harrison, and D. Sweatman, Interfacial characteristics of N_2O and NO nitrided SiO_2 grown on SiC by rapid thermal processing, Appl. Phys. Lett. **70**, 2028 (1997).

[11] G. Chung, C. Tin, J. Williams, K. McDonald, R. Chanana, R. Weller, S. Pantelides, L. Feldman, O. Holland, M. Das, and J. Palmour, Improved inversion channel mobility for 4H-SiC MOSFETs following high temperature anneals in nitric oxide, IEEE Electron Device Lett. **22**, 176 (2001).

[12] P. Deák, J. M. Knaup, T. Hornos, C. Thill, A. Gali, and T. Frauenheim, The mechanism of defect creation and passivation at the SiC/SiO_2 interface, J. Phys. D: Appl. Phys. **40**, 6242 (2007).

[13] F. Devynck, A. Alkauskas, P. Broqvist, and A. Pasquarello, Charge transition levels of carbon-, oxygen-, and hydrogen-related defects at the SiC/SiO_2 interface through hybrid functionals, Phys. Rev. B **84**, 235320 (2011).

[14] F. Devynck, A. Alkauskas, P. Broqvist, and A. Pasquarello, Defect levels of carbon-related defects at the SiC/SiO_2 interface from hybrid functionals, Phys. Rev. B **83**, 195319 (2011).

[15] K. Puschkarsky, T. Grasser, T. Aichinger, W. Gustin, and H. Reisinger, in *2018 IEEE International Reliability Physics Symposium (IRPS)* (IEEE, Burlingame, CA, USA, 2018), p. 1.

[16] K. Puschkarsky, H. Reisinger, T. Aichinger, W. Gustin, and T. Grasser, in *2017 IEEE International Integrated Reliability Workshop (IIRW)* (IEEE, South Lake Tahoe, CA, USA, 2017), p. 1.

[17] C. Schleich, D. Waldhoer, K. Waschneck, M. W. Feil, H. Reisinger, T. Grasser, and M. Waltl, Physical modeling of charge trapping in 4H-SiC DMOSFET technologies, IEEE Trans. Electron Devices **68**, 4016 (2021).

[18] K. Huang and A. Rhys, Theory of light absorption and non-radiative transitions in F-centres, R. Soc. **204**, 406 (1950).

[19] M. Kirton and M. Uren, Noise in solid-state microstructures: A new perspective on individual defects, interface states and low-frequency ($1/f$) noise, Adv. Phys. **38**, 367 (1989).

[20] W. Goes, Y. Wimmer, A.-M. El-Sayed, G. Rzepa, M. Jech, A. Shluger, and T. Grasser, Identification of oxide defects in semiconductor devices: A systematic approach linking DFT to rate equations and experimental evidence, Microelectron. Reliab. **87**, 286 (2018).

[21] A. Vasilev, M. W. Feil, C. Schleich, B. Stampfer, G. Rzepa, G. Pobegen, T. Grasser, and M. Waltl, Oxide and interface defect analysis of lateral 4H-SiC MOSFETs through CV characterization and TCAD simulations, Mater. Sci. Forum **1090**, 119 (2023).

[22] T. Aichinger, M. W. Feil, and P. Salmen, Assessing, controlling and understanding parameter variations of SiC power MOSFETs in switching operation, Key Eng. Mater. **947**, 69 (2023).

[23] M. W. Feil, K. Waschneck, H. Reisinger, P. Salmen, G. Rescher, T. Aichinger, W. Gustin, and T. Grasser, On the frequency dependence of the gate switching instability in silicon carbide MOSFETs, Mater. Sci. Forum **1092**, 109 (2023).

[24] M. W. Feil, K. Waschneck, H. Reisinger, J. Berens, T. Aichinger, P. Salmen, G. Rescher, W. Gustin, and T. Grasser, in *2023 IEEE International Reliability Physics Symposium (IRPS)* (IEEE, Monterey, CA, USA, 2023), p. 1.

[25] T. Grasser, P.-J. Wagner, P. Hehenberger, W. Goes, and B. Kaczer, A rigorous study of measurement techniques for negative bias temperature instability, IEEE Trans. Device Mater. Reliab. **8**, 526 (2008).

[26] M. E. Bathen, C. T.-K. Lew, J. Woerle, C. Dorfer, U. Grossner, S. Castelletto, and B. C. Johnson, Characterization methods for defects and devices in silicon carbide, J. Appl. Phys. **131**, 140903 (2022).

[27] R. Stahlbush, P. Macfarlane, J. Williams, G. Chung, L. Feldman, and K. McDonald, Light emission from 4H SiC MOSFETs with and without NO passivation, Microelectron. Eng. **59**, 393 (2001).

[28] R. E. Stahlbush and P. J. Macfarlane, Light emission from interface traps and bulk defects in SiC MOSFETs, J. Electron. Mater. **30**, 188 (2001).

[29] P. J. Macfarlane and R. E. Stahlbush, Characterization of light emission from 4H and 6H SiC MOSFETs, OPL **640**, 49 (2000).
[30] M. W. Feil, H. Reisinger, A. Kabakow, T. Aichinger, C. Schleich, A. Vasilev, D. Waldhör, M. Waltl, W. Gustin, and T. Grasser, Electrically stimulated optical spectroscopy of interface defects in wide-bandgap field-effect transistors, Commun. Eng. **2**, 5 (2023).
[31] M. W. Feil, H. Reisinger, A. Kabakow, T. Aichinger, W. Gustin, and T. Grasser, in *2022 IEEE International Reliability Physics Symposium (IRPS)* (IEEE, Dallas, TX, USA, 2022), p. 1.
[32] M. Weger, M. W. Feil, M. V. Orden, J. Cottom, M. Bockstedte, and G. Pobegen, Temperature-dependent electroluminescence of a gate pulsed silicon carbide metal-oxide-semiconductor field-effect transistor: Insight into interface traps, J. Appl. Phys. **134**, 034503 (2023).
[33] M. Weger, D. Biermeier, M. W. Feil, J. Cottom, M. Bockstedte, and G. Pobegen, Electroluminescence spectra of a gate switched MOSFET at cryogenic and room temperatures agree with ab initio calculations of 4H-SiC/SiO_2-interface defects, Mater. Sci. Forum **1091**, 15 (2023).
[34] R. Weingärtner, P. J. Wellmann, M. Bickermann, D. Hofmann, T. L. Straubinger, and A. Winnacker, Determination of charge carrier concentration in n- and p-doped SiC based on optical absorption measurements, Appl. Phys. Lett. **80**, 70 (2002).
[35] H. Reisinger, O. Blank, W. Heinrigs, A. Muhlhoff, W. Gustin, and C. Schlunder, in *2006 IEEE International Reliability Physics Symposium Proceedings (IRPS)* (IEEE, San Jose, CA, USA, 2006). p. 448.
[36] J. Mooney and P. Kambhampati, Get the basics right: Jacobian conversion of wavelength and energy scales for quantitative analysis of emission spectra, J. Phys. Chem. Lett. **4**, 3316 (2013).
[37] G. Susinni, S. Rizzo, F. Iannuzzo, and A. Raciti, A non-invasive SiC MOSFET junction temperature estimation method based on the transient light emission from the intrinsic body diode, Microelectron. Reliab. **114**, 113845 (2020).
[38] L. A. Ruppert, M. Laumen, and R. W. D. Doncker, in *24th European Conference on Power Electronics and Applications (EPE'22 ECCE Europe)* (IEEE, Hanover, Germany, 2022), p. 1.
[39] N. Kuznetsov and A. Zubrilov, Deep centers and electroluminescence in 4H SiC diodes with a p-type base region, Mater. Sci. Eng.: B **29**, 181 (1995).
[40] P. B. Klein, B. V. Shanabrook, S. W. Huh, A. Y. Polyakov, M. Skowronski, J. J. Sumakeris, and M. J. O'Loughlin, Lifetime-limiting defects in n^- 4H-SiC epilayers, Appl. Phys. Lett. **88**, 052110 (2006).
[41] F. Fabbri, D. Natalini, A. Cavallini, T. Sekiguchi, R. Nipoti, and F. Moscatelli, Comparison between cathodoluminescence spectroscopy and capacitance transient spectroscopy on Al^+ ion implanted 4H-SiC p^+/n diodes, Superlattices. Microstruct. **45**, 383 (2009).
[42] S. Bishop, C. Reynolds, J. Molstad, F. Stevie, D. Barnhardt, and R. Davis, On the origin of aluminum-related cathodoluminescence emissions from sublimation grown 4H-SiC($11\bar{2}0$), Appl. Surf. Sci. **255**, 6535 (2009).
[43] A. Fissel, W. Richter, J. Furthmüller, and F. Bechstedt, On the nature of the D1-defect center in SiC: A photoluminescence study of layers grown by solid-source molecular-beam epitaxy, Appl. Phys. Lett. **78**, 2512 (2001).
[44] M. D. McCluskey, Local vibrational modes of impurities in semiconductors, J. Appl. Phys. **87**, 3593 (2000).
[45] G. Groeseneken, H. Maes, N. Beltran, and R. D. Keersmaecker, A reliable approach to charge-pumping measurements in MOS transistors, IEEE Trans. Electron Devices **31**, 42 (1984).
[46] A. Salinaro, G. Pobegen, T. Aichinger, B. Zippelius, D. Peters, P. Friedrichs, and L. Frey, Charge pumping measurements on differently passivated lateral 4H-SiC MOSFETs, IEEE Trans. Electron Devices **62**, 155 (2015).
[47] J. Serrano, J. Strempfer, M. Cardona, M. Schwoerer-Böhning, H. Requardt, M. Lorenzen, B. Stojetz, P. Pavone, and W. J. Choyke, Determination of the phonon dispersion of zinc blende (3C) silicon carbide by inelastic x-ray scattering, Appl. Phys. Lett. **80**, 4360 (2002).
[48] J. Serrano, J. Strempfer, M. Cardona, M. Schwoerer-Böhning, H. Requardt, M. Lorenzen, B. Stojetz, P. Pavone, and W. J. Choyke, Lattice dynamics of 4H-SiC by inelastic x-ray scattering, Mater. Sci. Forum **433-436**, 257 (2003).
[49] S. Deng, C. Xiao, J. Yuan, D. Ma, J. Li, N. Yang, and H. He, Thermal boundary resistance measurement and analysis across SiC/SiO_2 interface, Appl. Phys. Lett. **115**, 101603 (2019).
[50] J. W. Steeds and W. Sullivan, Identification of antisite carbon split-interstitial defects in 4H-SiC, Phys. Rev. B **77**, 195204 (2008).
[51] A. Mattausch, M. Bockstedte, O. Pankratov, J. W. Steeds, S. Furkert, J. Hayes, W. Sullivan, and N. G. Wright, High energy local vibrational modes of carbon aggregates in SiC: Experimental and theoretical insight, Mater. Sci. Forum **527–529**, 465 (2006).
[52] A. Mattausch, M. Bockstedte, and O. Pankratov, Structure and vibrational spectra of carbon clusters in SiC, Phys. Rev. B **70**, 235211 (2004).
[53] M. Bockstedte, A. Mattausch, and O. Pankratov, Ab initio study of the annealing of vacancies and interstitials in cubic SiC: Vacancy-interstitial recombination and aggregation of carbon interstitials, Phys. Rev. B **69**, 235202 (2004).
[54] P. Li, P. Udvarhelyi, S. Li, B. Huang, and A. Gali, Carbon cluster emitters in silicon carbide, Phys. Rev. B **108**, 085201 (2023).
[55] A. Gali, P. Deák, P. Ordejón, N. T. Son, E. Janzén, and W. J. Choyke, Aggregation of carbon interstitials in silicon carbide: A theoretical study, Phys. Rev. B **68**, 125201 (2003).
[56] J. W. Steeds, S. Furkert, J. Hayes, and W. Sullivan, Low temperature annealing of optical centres in 4H SiC, Mater. Sci. Forum **457-460**, 637 (2004).
[57] T. Kobayashi and T. Kimoto, Carbon ejection from a SiO_2/SiC(0001) interface by annealing in high-purity Ar, Appl. Phys. Lett. **111**, 062101 (2017).
[58] J. Woerle, B. C. Johnson, R. Stark, M. Camarda, and U. Grossner, Fast defect mapping at the SiO_2/SiC interface using confocal photoluminescence, Mater. Sci. Forum **1062**, 389 (2022).
[59] B. Johnson, J. Woerle, D. Haasmann, C.-K. Lew, R. Parker, H. Knowles, B. Pingault, M. Atature, A. Gali, S. Dimitrijev,

M. Camarda, and J. McCallum, Optically active defects at the SiC/SiO_2 interface, Phys. Rev. Appl. **12**, 044024 (2019).

[60] Y. Abe, T. Umeda, M. Okamoto, R. Kosugi, S. Harada, M. Haruyama, W. Kada, O. Hanaizumi, S. Onoda, and T. Ohshima, Single photon sources in 4H-SiC metal-oxide-semiconductor field-effect transistors, Appl. Phys. Lett. **112**, 031105 (2018).

[61] A. Lohrmann, N. Iwamoto, Z. Bodrog, S. Castelletto, T. Ohshima, T. Karle, A. Gali, S. Prawer, J. McCallum, and B. Johnson, Single-photon emitting diode in silicon carbide, Nat. Commun. **6**, 7783 (2015).

[62] A. Lohrmann, S. Castelletto, J. R. Klein, T. Ohshima, M. Bosi, M. Negri, D. W. M. Lau, B. C. Gibson, S. Prawer, J. C. McCallum, and B. C. Johnson, Activation and control of visible single defects in 4H-, 6H-, and 3C-SiC by oxidation, Appl. Phys. Lett. **108**, 021107 (2016).

[63] J. Woerle, B. C. Johnson, C. Bongiorno, K. Yamasue, G. Ferro, D. Dutta, T. A. Jung, H. Sigg, Y. Cho, U. Grossner, and M. Camarda, Two-dimensional defect mapping of the SiO_2/4H-SiC interface, Phys. Rev. Mater. **3**, 084602 (2019).

[64] N. Alyabyeva, J. Ding, M. Sauty, J. Woerle, Y. Jousseaume, G. Ferro, J. C. McCallum, J. Peretti, B. C. Johnson, and A. C. H. Rowe, Nanoscale mapping of sub-gap electroluminescence from step-bunched, oxidized 4H-SiC surfaces, Phys. Status Solidi (b) **260**, 2200356 (2022).

[65] Y. Yamagishi and Y. Cho, Nanosecond microscopy of capacitance at SiO_2/4H-SiC interfaces by time-resolved scanning nonlinear dielectric microscopy, Appl. Phys. Lett. **111**, 163103 (2017).

[66] S. E. Schwartz, The Franck-Condon principle and the duration of electronic transitions, J. Chem. Educ. **50**, 608 (1973).

[67] L. Razinkovas, M. W. Doherty, N. B. Manson, C. G. V. de Walle, and A. Alkauskas, Vibrational and vibronic structure of isolated point defects: The nitrogen-vacancy center in diamond, Phys. Rev. B **104**, 045303 (2021).

[68] F. Yan, R. P. Devaty, W. J. Choyke, A. Gali, T. Kimoto, T. Ohshima, and G. Pensl, Anharmonic vibrations of the dicarbon antisite defect in 4H-SiC, Appl. Phys. Lett. **100**, 132107 (2012).

[69] P. M. Morse, Diatomic molecules according to the wave mechanics. II. Vibrational levels, Phys. Rev. **34**, 57 (1929).